ACS Catalysis

Research Article

pubs.acs.org/acscatalysis

Cu Nanoparticles Inlaid Mesoporous Al_2O_3 As a High-Performance Bifunctional Catalyst for Ethanol Synthesis via Dimethyl Oxalate Hydrogenation

Yifeng Zhu,[†,‡] Xiao Kong,[†,‡] Xianqing Li,[§] Guoqiang Ding,[§] Yulei Zhu,[*,†,§] and Yong-Wang Li[†,§]

[†]State Key Laboratory of Coal Conversion, Institute of Coal Chemistry, Chinese Academy of Sciences, Taiyuan 030001, Peoples' Republic of China

[‡]University of Chinese Academy of Sciences, Beijing 100039, Peoples' Republic of China

[§]Synfuels China Co. Ltd, Beijing, 101407, Peoples' Republic of China

Supporting Information

ABSTRACT: Ethanol synthesis from syngas via dimethyl oxalate (DMO) hydrogenation is of crucial importance for environment- and energy-related applications. Herein, we designed the bifunctional Cu nanoparticle (NP) inlaid mesoporous Al_2O_3 catalyst and first applied it to ethanol synthesis with high efficiency. The catalyst was made based on the spatial restriction strategy by pinning the Cu NPs on mesoporous Al_2O_3 to conquer the sintering problem and facilitate the stability (>200 h at 270 °C), which has potential values in high-temperature and exothermic reactions. The plentiful pores, highly exposed and properly assembled Cu-acid sites, furnished the catalyst with high ethanol yield (~94.9%). A structure-sensitive behavior that the intrinsic activity increases with the decreasing NP size was discussed. It was attributed to the change in metal−acid interfacial sites, morphology, and electronic structure and balance of surface Cu^0−Cu^+ species. The mechanism for DMO hydrogenation to ethanol involving activation of C═O, C−O, and O−H bands was also proposed. As cleavage of these bonds is a versatile tool to utilize bioderived molecules (e.g., polyols), the bifunctional catalysts can also be applied to hydrogenolysis of C−O bonds or etherification of O−H groups to produce various chemicals.

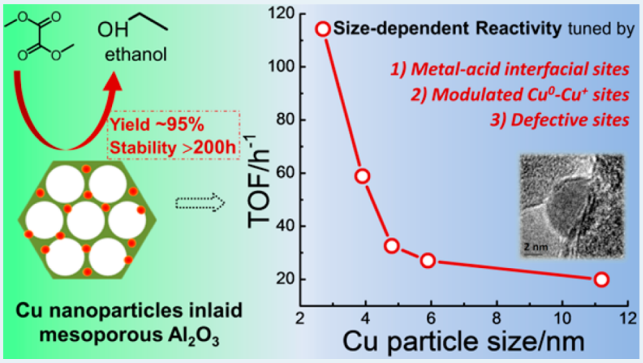

KEYWORDS: *ethanol synthesis, copper, mesoporous Al_2O_3, stability, metal-acid, structure−activity relationship*

1. INTRODUCTION

Ethanol is a good candidate for fuel cells and alternative fuels with little environmental hazard.[1−3] Currently, it is mainly produced from ethylene hydration and fermentation of sugars, which were limited by the shrinking oil and expensive bioprocesses.[4−6] Syngas can be obtained from versatile materials such as fossil fuels (e.g., coal, natural gas, and naphtha), renewable biomass, and organic wastes.[7] Ethanol synthesis from syngas via DMO hydrogenation (Scheme 1) can therefore bridge the gap between the nonrenewable petroleum route and costly biofermentation with low waste, cost, and energy consumption. This emerging technology includes syngas production, CO oxidative coupling to DMO, and subsequent hydrogenation to ethanol, among which the first two steps have been industrialized.[8,9] In the case of DMO hydrogenation, the Cu-based catalyst was frequently used because of its high activity. Nevertheless, the key challenges for commercialization are the unsatisfied stability of Cu catalysts due to metal-particle aggregation under the highly exothermic DMO hydrogenation[8,10−12] and low ethanol selectivity due to the chain growth of C2 intermediates over basic sites and etherification of alcohols over acidic sites.[10,11] Herein, we highlight the catalyst design for improving the stability of Cu-based catalysts and the significant improvement in ethanol selectivity based on the understanding of the ethanol formation mechanism.

Pinning or partially embedding the metal NPs in thermally stable mesoporous materials is an appealing strategy to prevent particle aggregation for various applications (e.g., catalysis, electrode materials for capacitors, and solar cells).[13−15] Apart from morphologies and texture properties, catalysts can also be functionalized with additional sites (e.g., acid sites).[16] Ordered mesoporous alumina (OM-Al_2O_3) is nanostructured alumina with highly uniform channels and pore-size distributions,[17] moderate acidity, and excellent thermal stability.[18−20] It, as a catalytic support, has attracted intense interest since Yuan et al. reported a facile synthetic route.[17] Herein, the Cu NP inlaid mesoporous Al_2O_3 was fabricated using a facile one-pot method and first applied to synthesize ethanol (Scheme 1). The rich

Received: March 3, 2014
Revised: September 1, 2014
Published: September 4, 2014

   dx.doi.org/10.1021/cs5009283 | ACS Catal. 2014, 4, 3612−3620

Scheme 1. Illustration for Ethanol Synthesis over Cu NPs Inlaid Mesoporous Al_2O_3

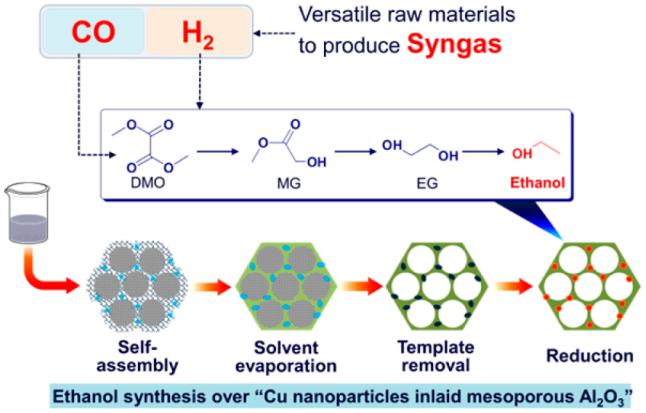

pores and strongly fixed Cu NPs embedded in the alumina wall immobilized the active sites and prevented metal sintering effectively and, thus, endowed the catalyst with remarkable stability (>200 h at 270 °C). The strategy demonstrated here has potential feasibility in other high-temperature or exothermic reactions.

Ethanol formation from DMO hydrogenation is comprised of the hydrogenation of C═O bonds in DMO and subsequent cleavage of C−O bonds in ethylene glycol (EG). Excessive basicity or acidity of catalysts would induce side reactions and reduce the ethanol selectivity. Properly assembled metal−acid sites may facilitate cleavage of C═O and C−O bonds as reported in our previous work, which eliminates the unwanted reactions over basic sites.[11] The acid sites over the Al_2O_3 surface would be expected to catalyze the dehydration of hydroxyl groups while the metal sites would be expected to hydrogenate the unsaturated intermediates into ethanol. However, the side reactions (e.g., etherification, especially the formation of 2-methoxyethanol (2-ME) between ethylene glycol and traditional methanol solvent) could also be catalyzed by acid sites.[11] A good solution to suppress the side reactions is to choose an inert solvent (e.g., 1,4-dioxane). By assembling proper Cu−acid sites and using 1,4-dioxane as a solvent, we received a high ethanol yield (~94.9%) over the Cu NP inlaid mesoporous Al_2O_3 catalyst.

Ethanol formation from DMO hydrogenation involves the C═O, C−O, and O−H activation over metal−acid sites and represents a wide range of reactions. The size−activity relationship (a case of structure-sensitive behaviors) in which the catalytic performance is greatly influenced by metal NP size is one essential issue in heterogeneous catalysis.[21−24] To facilitate further studies, the reaction mechanism governing ethanol generation was discussed, as well as the size-sensitive behavior. In addition, the vicinal OH groups of EG represent a ubiquitous feature of bioderived carbohydrates.[25] Based on the understanding in selective activation of C−O and O−H bonds here, the catalysts can also be applied to hydrogenolysis and etherification reactions of polyols to produce various chemicals.

2. EXPERIMENTAL SECTION

2.1. Chemicals. Pluronic P123 (M = 5800) was purchased from Sigma-Aldrich; aluminum iso-propoxide, HNO_3 (67 wt %), ethanol, and cupric nitrate trihydrate were purchased from Sinopharm Chemical Reagents. These reagents were used as received without further purification.

2.2. Catalyst Preparation and Evaluation. In a typical procedure, 1.0 g of P123 was dissolved with 20 mL of ethanol at ambient temperature; then 1.5 mL of nitric acid and 10 mmol of metal precursors (aluminum iso-propoxide and cupric nitrate trihydrate with designed proportion) were added. The mixture was stirred for 12 h and then dried at 60 °C for 48 h. The as-synthesized precursor was calcined at 450 °C for 5 h in the air. The final samples were labeled in the general form of xCuyAl with x and y indicating the Cu and Al molar percentages, respectively. The reference Cu/mesoporous Al_2O_3 catalyst was prepared using the incipient impregnation method (Cu/Al = 15/85 mol/mol). The evaluations, except hydrogenolysis of 1,2-propanol and 1,2,6-hexanetriol, were performed in a fixed-bed reactor after the catalysts (20−40 meshes) were in situ activated with a H_2 flow at 250 °C; hydrogenolysis of 1,2-propanol and 1,2,6-hexanetriol was tested in a 100 mL autoclave with an inserted Teflon vessel. Details of the reaction conditions are presented below each results. The liquid products of fixed-bed tests were condensed in a cold trap. All the liquid products were analyzed using a gas chromatograph (DB-WAXETR column) equipped with a FID detector and identified by a GC/MS instrument. The gaseous products of fix-bed tests were analyzed using an online gas chromatograph (HP-INOWAX column) equipped with a FID detector and an online gas chromatograph (HP-MoleSieve 5A column) equipped with a TCD detector. The products were determined quantitatively by calibrated area normalization.

2.3. Characterization. The composition of the samples was determined by ICP optical emission spectroscopy (Optima2100DV, PerkinElmer). The thermal gravimetric analysis (TG) experiments were performed on a Mettler Toledo TGA/DSC-1 instrument in the range of 30 to 900 °C and under an air atmosphere (60 mL/min). The N_2 adsorption−desorption isotherms at −196 °C were measured using an ASAP 2420 analyzer (Micromeritics Co. Ltd.) after the catalysts were degassed at 350 °C for 8 h. Temperature-programmed reduction (TPR), temperature-programmed desorption of NH_3 (NH_3-TPD), and N_2O chemisorption experiments were carried out on an Auto Chem II 2920 (Micromeritics, USA). Wide-angle powder X-ray diffraction patterns in the range of 10° to 90° and low-angle powder X-ray diffraction patterns in the range of 0.4° to 6° were recorded on a Rigaku D/MAX-2000 diffractometer (step size of 0.02°, count time of 0.5 s) and a Bruker D8-advance diffractometer (step size of 0.02°, count time of 4 s) with Cu Kα radiation, respectively. Raman spectra of the catalysts were determined by a LabRAM HR800 system equipped with a CCD detector at room temperature; the 325 nm of the He−Cd laser was used as the exciting source with a power of 30 MW. A 60% reduction of laser output was chosen for the samples to ensure that the samples were not damaged. The power of the laser at the sample (~0.4 mW) was measured by an optical power meter (Thorlabs PM 100D) equipped with S120VC photodiode power sensor. The IR and Pyridine adsorbed IR (Py-IR) spectra of powder samples were recorded with a Vertex 70 (Bruker) FTIR spectrophotometer in the range of 4000−400 cm^{-1} at a resolution of 4 cm^{-1}. TEM, dark-field scanning TEM (STEM), and energy dispersive X-ray spectroscopy (EDX) measurements were carried out on a JEM-2100F high-resolution transmission operated at 200 keV. X-ray photoelectron spectroscopy (XPS) was performed on a Thermo XPS ESCALAB 250Xi spectrometer equipped with a monochromatic Al Kα (1486.8 eV) source. The XPS experiments of reduced samples were performed after an in situ reduction at 250 °C for 2 h. More details could be found in the Supporting Information.

3. RESULTS AND DISCUSSION

3.1. Catalytic Performance of xCuyAl Catalysts for Ethanol Synthesis. Table 1 summarizes the catalytic performance of the xCuyAl catalysts for ethanol synthesis via DMO hydrogenation. To facilitate the ethanol formation, both the hydrogenation of ester groups and the hydrogenolysis of C−O bonds need to be promoted. The tests were therefore performed at high temperature (270 °C) and high H_2 pressure. All the catalysts exhibited excellent activity with 100% DMO

dx.doi.org/10.1021/cs5009283 | ACS Catal. 2014, 4, 3612−3620

Table 1. Catalytic Performance of *x*Cu*y*Al Catalysts[a]

		sel. (%)[b]				
catalysts	conv. (%)	ethanol	EG	2-ME	others	TOFs (h^{-1})[c]
2Cu98Al	100	56.3	0.1	22.2	21.4	114.2
5Cu95Al	100	68.1	0	17.2	14.7	58.8
10Cu90Al	100	77.3	0.2	14.4	8.1	32.6
15Cu85Al	100	94.3	0	3.7	2.0	27.0
20Cu80Al	100	94.9	0	3.6	1.5	19.8

[a]Reaction conditions: 270 °C, 4 MPa, liquid hourly space velocity (LHSV) = 0.2 h^{-1}, H_2/DMO = 200, 15 wt % DMO/1,4-dioxane as feed. [b]Others mainly consist of methyl glycolate (MG), diglycol, diglyme, and some other related ethers; see Supporting Information for the calculation of selectivity. [c]Turnover frequencies (TOFs), see Supporting Information for details.

conversion. Among them, both 15Cu85Al and 20Cu80Al exhibited high ethanol selectivity of ~95%. It is noted that increasing Cu loading concurrently suppressed the 2-ME formation and brought out a significant improvement in ethanol selectivity. The reference Cu/mesoporous Al_2O_3 catalyst was also prepared by the impregnation method (Table S1 and Figure S1). The catalyst exhibited an ethanol yield of 83.2%, much lower than that of 15Cu85Al. The results demonstrated the superior ability of the one-pot method for dispersing/incorporating Cu NPs into the mesoporous Al_2O_3.

Turnover frequencies (TOFs) were calculated by dividing the catalytic performance by Cu surface area according to the previous study.[8] To obtain the intrinsic activity of catalysts, DMO conversion was kept below 50%, and ethanol yield was kept below 10% at a high liquid hour space velocity of 9 h^{-1} (Table S2). Interestingly, TOFs decreased with the increasing Cu loading and diameter of Cu NPs (Table 2), revealing a strong structure-sensitive behavior which will be discussed below. Considering the possible contribution of solvent 1,4-dioxane to ethanol selectivity, the blank 1,4-dioxane and 15 wt % DMO/tetrahydrofuran were fed respectively (see Table S3 for details). It was found that 1,4-dioxane solvent was almost unchangeable under the reaction conditions. Given that 1,4-dioxane can suppress the side reactions and has lower toxicity than methanol, it would be a better choice for ethanol synthesis than the traditional methanol solvent (see Table S4 for details).

The 15Cu85Al catalyst was selected to investigate the long-term stability for ethanol synthesis (Figure 1). Almost constant DMO conversion (100%) and ethanol selectivity (~94.5%) for 200 h tests under high temperature (270 °C) indicated the high stability of the catalyst. Cu NPs over the used catalysts were not sintered from the TEM results (Figure S2), providing evidence for the superior stability of the catalyst. The preserved mesoporous structures and "mosaic structure" of Cu NPs in

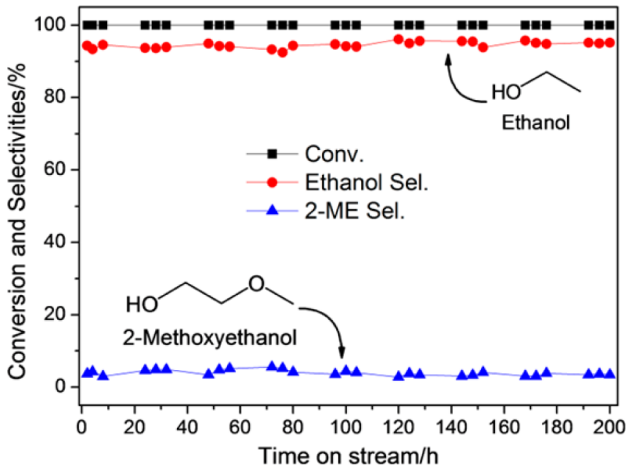

Figure 1. DMO conversion and ethanol selectivity versus time on stream (reaction conditions: 15Cu85Al, 270 °C, 4 MPa, LHSV = 0.2 h^{-1} H_2/DMO = 200).

the alumina walls may suppress the copper aggregation and facilitate stability.

The Cu NP inlaid mesoporous Al_2O_3 realized superior selectivity among the catalysts reported[8,10] and possessed higher stability than the coprecipitated Cu/Al_2O_3 catalyst in our previous work (270 °C, 80 h),[11] revealing promising applications for indirect synthesis of ethanol from syngas. The space restriction via partially embedding the Cu NPs over mesoporous Al_2O_3 walls overcame the metal aggregation and deactivation problems of catalysts (e.g., the Cu/Al_2O_3 catalyst prepared by coprecipitation[11]).

3.2. Characterizations of *x*Cu*y*Al Catalysts. Table 2 presents the main physicochemical properties of the OM-Al_2O_3 and as-prepared catalysts. The actual copper contents are slightly lower than the nominal values, because of the residual carbon species (the residence of template P123; Figure S3 and Table S5). From N_2O titration results, excellent copper dispersions were exhibited in the composites, but the dispersions gradually decreased at higher Cu contents. Despite the decrease in Cu dispersion, higher Cu surface areas were obtained by increasing Cu loadings. The elevated Cu content also resulted in a decrease of pore volume and BET surface area, as well as pore expansion. N_2 adsorption isotherms and the corresponding pore size distributions are shown in Figure 2. The uniformity of mesopores is supported by type IV isotherms with H1 hysteresis loops and steep capillary condensation steps when the Cu content is lower than 15%. With a further increase of Cu loading, the steepness of the capillary condensation steps drops quickly and the pores expand. Disordered large

Table 2. Main Physicochemical Properties of As-Prepared Catalysts

entry	loading (wt %)[a]	D_{Cu} (%)[b]	S_{Cu} (m^2/g)[b]	S_{BET} (m^2/g)[c]	V_p (cm^3/g)[c]	d_p (nm)[c]	d_{Cu} (nm)[d]	D_{Cu} (%)[d]	total acidity (mmol NH_3/g cat.)[e]
OM-Al_2O_3				304.5	0.56	6.1			2.55×10^{-2}
2Cu98Al	1.98	10.3	1.4	232.7	0.52	7.1	2.7	41.9	2.33×10^{-2}
5Cu95Al	5.01	9.9	3.4	228.6	0.45	5.3	3.9	30.6	2.33×10^{-2}
10Cu90Al	10.16	9.3	6.4	167.4	0.36	7.4	4.8	25.4	2.30×10^{-2}
15Cu85Al	14.67	8.0	7.9	100.3	0.29	6.1	5.9	19.2	1.76×10^{-2}
20Cu80Al	21.35	7.1	10.3	52.6	0.19		11.2	13.2	1.12×10^{-2}

[a]Copper loadings were measured by ICP-OES. [b]Cu dispersion and Cu surface area were determined by N_2O titration. [c]The BET surface area, pore volume, and pore size were determined by N_2 physical adsorption. [d]Diameter of Cu NPs and Cu dispersion were calculated based on statistical results (see Supporting Information) of TEM images (Figure S5). [e]Amount of acid sites was estimated by NH_3-TPD.

dx.doi.org/10.1021/cs5009283 | ACS Catal. 2014, 4, 3612−3620

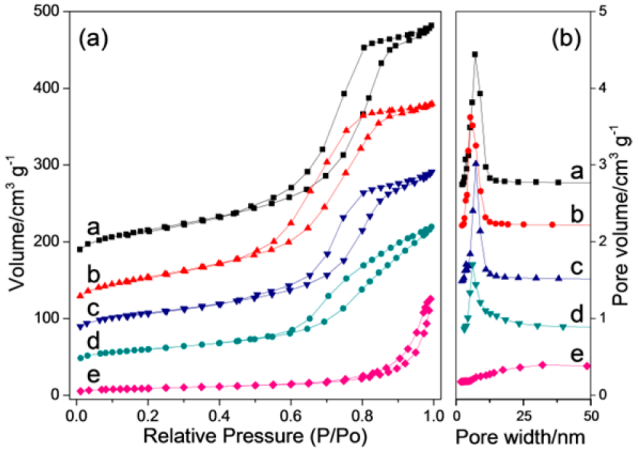

Figure 2. Adsorption isotherms (a) and pore size distributions (b) of *x*Cu*y*Al catalysts (a, 2Cu98Al; b, 5Cu95Al; c, 10Cu90Al; d,: 15Cu85Al; e, 20Cu80Al).

mesopores with an H3 hysteresis loop were observed for the 20Cu80Al catalyst, indicating that the ordered structures collapsed with excessive copper.

The low-angle and wide-angle XRD (inset) patterns for as-prepared samples are displayed in Figure 3. OM-Al_2O_3

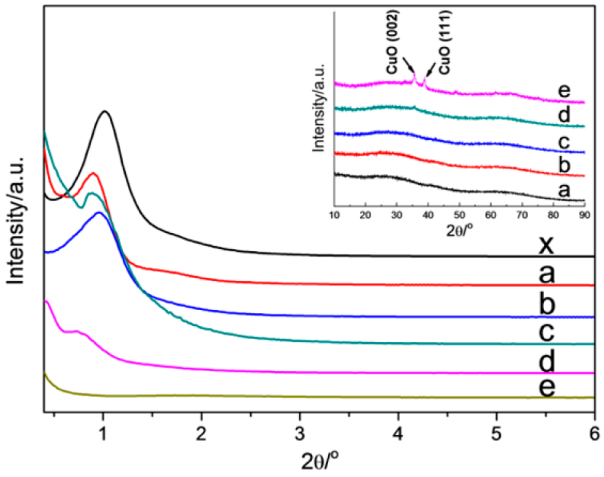

Figure 3. Small-angle XRD and wide-angle XRD patterns of *x*Cu*y*Al catalysts (a, 2Cu98Al; b, 5Cu95Al; c, 10Cu90Al; d, 15Cu85Al; e, 20Cu80Al; x, OM-Al_2O_3).

presented an intensive peak around 1° that corresponds to the (100) diffraction of the hexagonal symmetry structure, indicating the presence of ordered mesopores.[19] However, the intensity of the (100) peak decreased with the increasing Cu loading, indicating that the ordered mesoporous structure is preserved upon Cu doping, but it will expand and collapse when Cu is excessively introduced into the framework. The results are consistent with the observations from N_2 adsorption experiments. From the wide-angle XRD patterns, broad CuO reflections are observed only when the Cu content exceeds 15%, revealing that an excellent Cu dispersion can be realized via the one-pot synthetic method. However, the broad/unobservable CuO reflections are unreliable for calculating the particle sizes of catalysts. We thus used the particle statistic method of TEM images as follows to determine the particle sizes. The absence of a diffraction peak of alumina indicated the X-ray amorphous state of support for all the catalysts.

Pore structures and elemental dispersions of the calcined catalysts were further investigated by electron microscopy measurements, as shown in Figure 4 and Figure S4. The

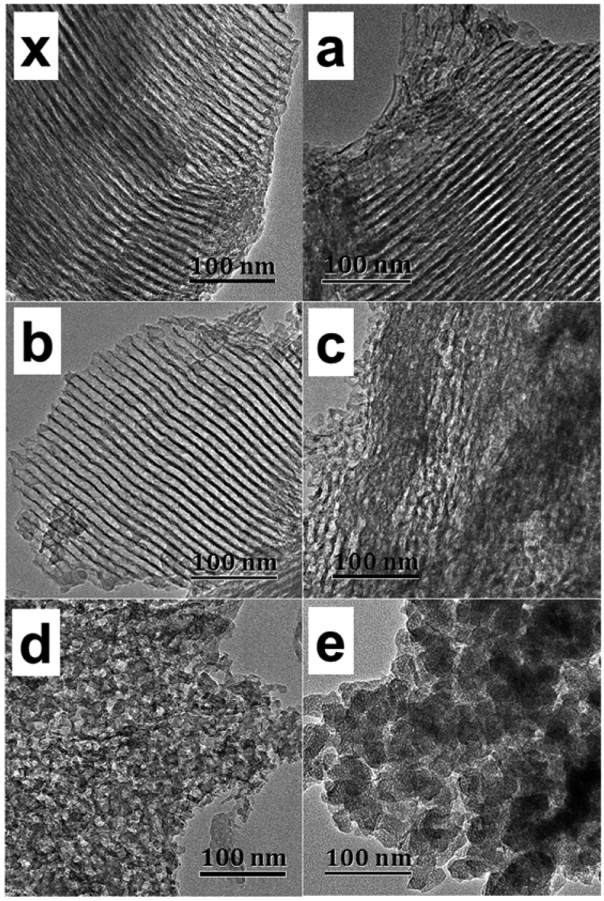

Figure 4. TEM images of unreduced *x*Cu*y*Al catalysts (a, 2Cu98Al; b, 5Cu95Al; c, 10Cu90Al; d, 15Cu85Al; e, 20Cu80Al; x, OM-Al_2O_3).

samples (doped Cu lower than 15%) possessed the ordered hexagonal arrays of mesopores. Upon further addition of Cu, the long-range periodical mesopores were destroyed into disordered worm-like pores. Although the added cupric nitrate would deteriorate the order in self-assembled composites, catalysts with proper Cu/Al ratios still provided many mesoporous structures. Because of the low Z-contrast between CuO and Al_2O_3 species, we used STEM-EDX to prove the porous morphology and homogeneous elemental dispersion. The ordered pores expanded and were damaged with the increase of Cu loadings (Figure S4), supporting the above results. The uniform distributions of Cu and Al elements over the composite matrixes demonstrated the superior dispersion ability of the one-pot method for multicomponent catalysts. After reduction, Cu NPs can be easily distinguished in HRTEM images taken from the edge of materials, except the 2Cu98Al catalyst (Figure S5). Cu NPs (dark spheres in HRTEM) were in intimate contact with the surrounding Al_2O_3, revealing that the well dispersed Cu NPs were immobilized in the amorphous alumina. In the case of 2Cu98Al catalyst, the small size of Cu NPs made it hard to measure the size distribution in HRTEM images. Thus, STEM was used to obtain the data (Figure S6). The average size of Cu NPs decreased while the Cu dispersion

dx.doi.org/10.1021/cs5009283 | *ACS Catal.* 2014, 4, 3612−3620

calculated based on the mean diameter increased with the lower Cu content (Table 2). Interestingly, the Cu dispersions calculated from TEM analysis were much higher than that of N_2O titration, confirming that the Cu NPs were partially embedded in Al_2O_3 walls.

The TPR profiles of the catalysts are shown in Figure 5, providing information on the states of CuO species. The

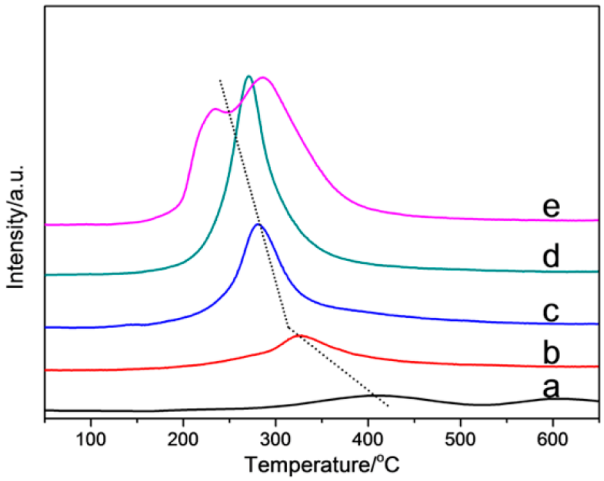

Figure 5. TPR profiles of *x*Cu*y*Al catalysts (a, 2Cu98Al; b, 5Cu95Al; c, 10Cu90Al; d, 15Cu85Al; e, 20Cu80Al).

locations of peaks gradually migrated toward the lower temperature at a higher Cu content, as well as the onset temperature of reduction. According to Behrens et al.,[26] the crystalline and pure CuO species are easier to reduce than the highly dispersed CuO in amorphous materials as a result of diffusion effects and the strong interactions between Cu species and Al_2O_3. The higher reduction temperature at lower Cu loading (<15%) indicated the presence of highly dispersed CuO species pinned in the mesoporous architectures. The mosaic structure of highly dispersed Cu NPs resulted in a superior stability of this Cu phase. A pronounced shoulder to the lower temperature side was observed over the 20Cu80Al catalyst, indicating different CuO species were formed with the collapse of ordered mesoporous structure. As confirmed by N_2 adsorption isotherms and the occurrence of CuO characteristics in XRD results, these species were large CuO particles which were not embedded in support. The TPR results rationalized the high performance of 15Cu85Al and further supported that the Cu NPs were highly dispersed and embedded in the amorphous mesoporous Al_2O_3 at a proper Cu loading.

To determine the state of Cu and Al species over the catalysts, FTIR and Raman measurements were performed (Figure S7). The OH groups of residual water and solvent gave rise to the bands of bending vibration at 1630 cm^{-1} and stretching vibration at 3470 cm^{-1}, respectively (Figure S7a).[27,28] Al ions occupied both tetrahedral (peak at 830 cm^{-1}) and octahedral (wide pattern in the 400−800 cm^{-1} range) sites in the oxygen anion sublattices.[29] With increasing Cu loadings, the structure changed from AlO_6 to the AlO_4 atomic group. The small shoulder band at 1050 cm^{-1} can be assigned to Al−OH structure, and it decreased in intensity with the increasing Cu/Al ratio.[29] Raman peaks around 297, 347, and 635 cm^{-1} correspond to the vibrations of Cu−O in the CuO lattice.[11] The broad bands in Raman spectra (Figure S7b) agreed with wide-angle XRD and EDX results, indicating the existence of highly dispersed CuO species.

Surface acidity was determined by NH_3-TPD (Figure 6) and FTIR spectra of pyridine adsorption (Figure S8). OM-Al_2O_3

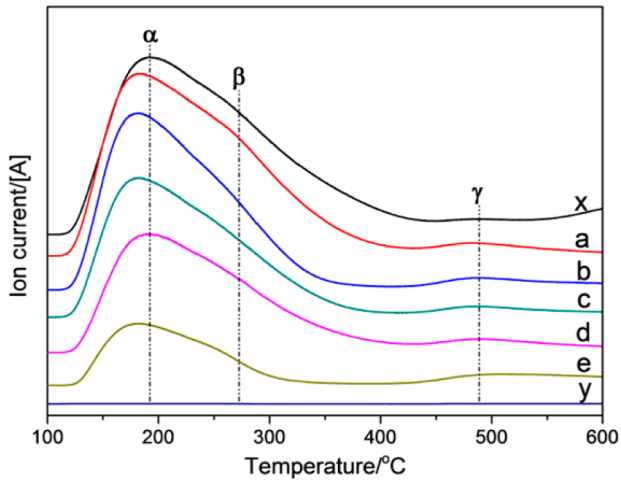

Figure 6. NH_3-TPD profiles of *x*Cu*y*Al catalysts and model catalysts (x, OM-Al_2O_3; a, 2Cu98Al; b, 5Cu95Al; c, 10Cu90Al; d, 15Cu85Al; e, 20Cu80Al; y, CuO ref).

and CuO reference (ref) were also tested. CuO ref was separated from the slurry of 15Cu85Al catalyst treated by NaOH solution. To exclude the influences of Na^+, the slurry was exchanged with dilute ammonia and washed with water 10 times. A main peak around 180 °C and a shoulder around 270 °C were observed for all the *x*Cu*y*Al catalysts, corresponding to the weak and medium acidic sites, respectively. A weak peak around 490 °C can be attributed to strong acidic sites.[28] The amount of acid sites diminished as a result of Cu doping. In addition, the straight line for CuO ref indicated that CuO species do not contribute to the acidity of the as-prepared catalysts. Characteristic adsorption bands at 1620 and 1450 cm^{-1} correspond to ν_{8a} and ν_{19b} modes of the ring-breathing vibrations $\nu_{(CCN)}$ of pyridine, respectively, indicating the adsorption via hydrogen-bonding with surface OH groups and the nitrogen-lone-pair electrons interacting with unsaturated Al^{3+} ions (Lewis acid sites).[17,30] The absence of a band at 1540 cm^{-1} indicated that the Brønsted acid sites were negligible over the catalysts. The amount of Lewis acid sites decreased gradually with the increasing Cu content, which was consistent with NH_3-TPD results.

The Cu 2p XP spectra of the calcined and reduced samples are shown in Figure S9. An evident Cu $2p_{3/2}$ peak at ∼933.3 eV, Cu $2p_{1/2}$ peak at ∼952.9 eV, and the 2p → 3d satellites between 942 and 948 eV were observed. The Cu sites existed as a Cu^{2+} state with a d^9 electron configuration over the calcined catalysts.[31] After the reduction process, the Cu^{2+} sites were converted into Cu^0 and/or Cu^+ sites, as evidenced by the absence of the Cu 2p satellite peaks at 942−948 eV and the shift of Cu 2p peaks toward lower binding energy. To distinguish the surface Cu^0−Cu^+ species, Cu LMM X-ray excited Auger spectroscopy was analyzed. The peaks of *x*Cu*y*Al catalysts varied by the Cu loadings. The appearance of two overlapping peaks at around 914 eV (Cu^+) and 918 eV (Cu^0) supported the existence of Cu^0−Cu^+ species (Figure S10).[32] The Cu^0 peaks emerged and intensified gradually with the elevation of Cu loadings. Deconvolution of the Cu LMM peaks

dx.doi.org/10.1021/cs5009283 | ACS Catal. 2014, 4, 3612−3620

was thus performed to determine the surface Cu^0/Cu^+ species (Figure 7). The *x*Cu*y*Al catalysts exhibited different $Cu^+/(Cu^0+Cu^+)$ ratios. The percentage of Cu^+ decreased gradually with the elevation of Cu loadings. The XPS results also confirmed the trend that the CuO species over catalysts with lower Cu contents were harder to reduce, which were in accordance with the TPR results.

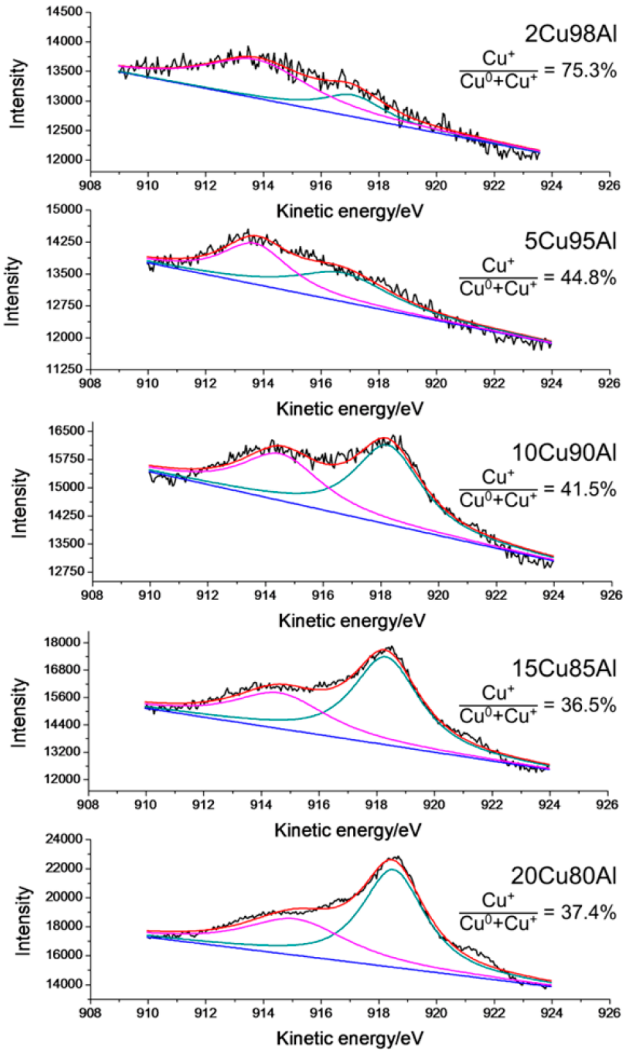

Figure 7. Deconvolution of Cu LMM X-ray excited Auger spectroscopy of reduced *x*Cu*y*Al catalysts.

On the basis of the above results, we demonstrated that the one-pot synthetic strategy is an effective and simple way to immobilize the highly dispersed Cu NPs into the skeleton of support. The above results suggested the following conclusions. (1) The ordered mesopores can be preserved with proper Cu doping, but the architectures would be deteriorated into worm-like pores with excessive Cu dopants; the nature of one-pot strategy and abundant pore structures may endow the catalysts with superior Cu dispersion. (2) The highly dispersed Cu NPs were inlayed into Al_2O_3 walls, exhibiting an excellent stability performance. (3) Because of the increase of Cu/Al ratio, the number of Cu sites increased with the diminishing of acid sites (only Lewis acid) while the ratios of $Cu^+/(Cu^0+Cu^+)$ decreased.

3.3. Reaction Mechanism and Size-Dependent Performance. Three model catalysts (15Cu85Al, CuO ref, OM-Al_2O_3) were evaluated to investigate ethanol formation over metal-acid sites (Table S6). Unsatisfied ethanol yields were observed over CuO ref and OM-Al_2O_3, while excellent ethanol yields were realized over the 15Cu85Al catalyst with either DMO or EG as the feed. The TOF of 15Cu85Al (27.0 h^{-1}) was much higher than that of CuO ref (~1.8 h^{-1}) for DMO hydrogenation to ethanol. The results demonstrated that both the Cu and Al_2O_3 sites are indispensable for the process.

Ethanol generation from DMO comprises several continuous reactions. The ethanol formation lies in the cooperative effect of metal and acid sites. For DMO hydrogenation to EG, the metallic Cu catalyzes the conversion of C═O bonds and C−O bonds in DMO to MG and EG step-by-step with the assistance of acid sites in activating these bonds.[32] The ethanol formation from EG can be explained by acid sites catalyzing the dehydration and metal sites acting as an active phase for hydrogenation processes (Scheme 2).[33,34] The acid sites

Scheme 2. Proposed Reaction Mechanism over Metal−Lewis Acid Active Sites (LA: Lewis Acid)

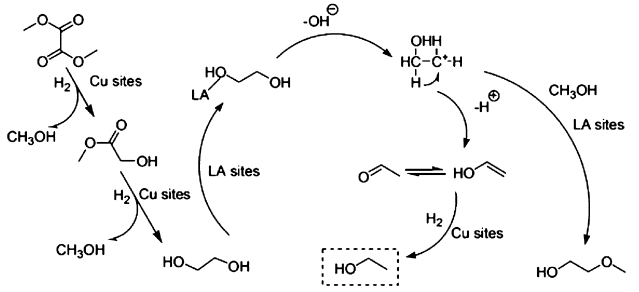

however will catalyze the dehydration-etherification of EG with methanol to form ethers (e.g., 2-ME) if hydrogenating ability of catalysts is not sufficient.[11] Thus, to access high ethanol selectivity and inhibit the side reactions over the metal−acid bifunctional catalysts, the traditional methanol solvent was replaced with aprotic 1,4-dioxane in our case.[11] Another feasible way for future investigations is to modify the metal sites and enhance the hydrogenation process.

In Figure 8a, we show the normalized Cu sites and acid sites as a function of Cu loading. With the elevated Cu loading, the trend in the two sites was a counterbalance: the number of metallic Cu sites increased with the diminishing of Lewis acid sites. The increase of surface Cu sites explained the enhanced ethanol yield at higher Cu/Al ratios. As shown in Figure 8b, the average Cu particle size increases and TOFs decrease as the Cu content mounts up. More remarkably, a strong size-dependent activity that TOFs decrease with increasing particle size emerged when we correlated the data above (Figure 8c). Similar structure−activity relationships have been observed over metal supported on different oxides.[24,35] A variation of Cu crystallite size would influence the copper−alumina interfacial sites, proportions of different types of surface atoms (planes, corner, and edge atoms), and electronic structure that governs the catalytic reactivity.[24,36−38]

The interfacial sites over catalysts are believed to provide a boost for the intrinsic activity.[24,39] Smaller particle size will lead to a larger fraction of interfacial sites. The ethanol formation is intrinsically linked with the metal and Lewis acid sites as mentioned above. At interfacial sites, the intermediate species

dx.doi.org/10.1021/cs5009283 | ACS Catal. 2014, 4, 3612−3620

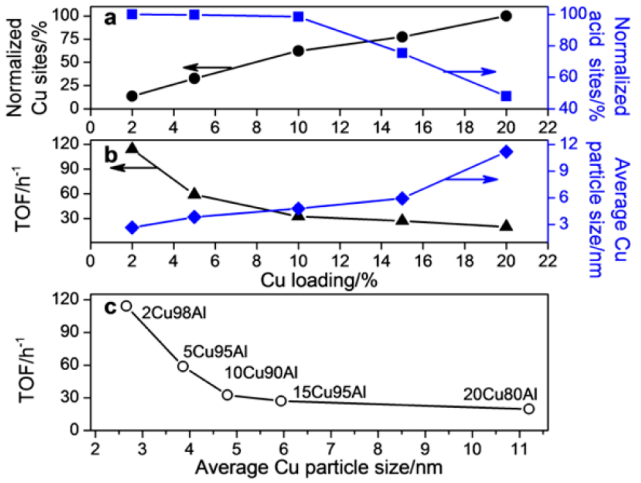

Figure 8. Normalized Cu and acid sites as a function of Cu loading (a, normalized: the highest sample = 100%); TOFs and average Cu particle size as a function of Cu loading (b); relation of the TOFs to the average Cu particle size (c).

diffused faster between metal and acid sites due to the minimized transport distances.[40] In addition, the different chemical environment of the interface caused by the strong interactions between Cu species and Al_2O_3 may also contribute to the activity. As proposed by Cargnello et al.,[24] the fraction of interfacial sites (including the perimeter and corner atoms in direct contact with the support) is proportional to the diameter (d) as $d^{-1.9\pm0.2} + d^{-2.6\pm0.1}$ for any regular solid other than a sphere. Cuboctahedron is the equilibrium shape at 0 K for fcc crystals (e.g., Cu, Ag, Au), as a result of thermodynamic considerations.[41] Thus, the smaller Cu particles are likely to contain more interfacial sites than larger ones. Although not conclusive, the role of copper−alumina interfacial sites may be a crucial factor.

Cu NP size also influences surface morphology and coordination states. Generally, smaller Cu NPs have more unsaturated atoms at open plane, edge, and corner sites.[35] Hydrogenation of CO/CO_2 (the models with C−O bonds) over Cu catalysts has emerged as a probe to demonstrate the structure sensitivity. Both the theoretical calculations and experiments supported that more open surfaces (e.g., (110), (100), (311) facets) are more active than a close-packed (111) surface.[42,43] Recently, Behrens et al.[44] found that Cu steps created by stacking faults, defects, and twin boundaries can stabilize intermediates and lower activation barriers, and thus increase the activity. Meanwhile, the electronic structure of Cu NPs was altered. The decreasing particle size would promote the proportion of surface atoms with lower coordination numbers and narrow the d-bandwidth, which would change the reactivity.[37,38] Apart from the interfacial sites and more open facets, the partially oxidized Cu sites are also suitable for reactions.[45] It has been suggested that Cu^0 species dissociate H_2, and Cu^+ sites function as electrophilic sites to polarize the carbonyl groups.[32] The balanced Cu^0 and Cu^+ sites can improve the activity for DMO hydrogenation.[8,12] The XPS results confirmed the existence of Cu^+ sites over the surface, of which the amount decreased with an increase of Cu loadings. Different from the Cu^0 sites at the surface, the oxidized Cu^+ species might be located at the boundaries of Cu NPs in contact with the support forming Cu−O bonds across the interface.[26] The Cu^0−Cu^+ synergy may be another factor for the size-dependent behavior.

In general, the apparent relationship between TOF and Cu NP size (the decreased trends of TOFs with the increase of Cu NPs size) can be attributed to the decreased proportion of Cu−Al_2O_3 interfacial sites, morphology, and electronic structure of Cu NPs and change of surface Cu^0−Cu^+ species by increasing particle size. For more quantitative conclusions, further studies would be needed.

3.4. Applications in Related Reactions for Converting Bioderived Chemicals. Growing demands for energy and chemicals have stimulated intense studies on catalytic utilization of biomass with high efficiency, low cost, and fewer environmental hazards. A case that has attracted particular interest is the conversion of polyols such as propylene glycol, glycerol, sorbitol, and monosaccharide with favorable activity and selectivity.[34] One key challenge is to selectively activate and cleave C−O and O−H bonds which are frequently catalyzed by copper and solid acid catalysts. EG, a basic unit for complex polyols, can be used as an ideal model for reactions of C−O and O−H bonds.[25] On the basis of the aforementioned mechanism, the metal−acid catalysts were extended to several cases of polyols to alter the activity and selectivity (Table 3, see the Supporting Information for reaction schemes).

Table 3. Performance of Catalysts for Model Reactions

reaction type	feed stocks	catalysts	conv. (%)	sel. (%)
etherification	EG/methanol	OM-Al_2O_3	100	65.8[a]
	EG/methanol	OM-Al_2O_3	100	81.2[b]
	DMO/methanol	2Cu98Al	100	66.9[c]
hydrogenolysis	EG/dioxane	15Cu85Al	100	97.0[d]
	1,2-propanol/dioxane	15Cu85Al	92.6	78.1[e]
	1,2,6-hexanetriol/water	15Cu85Al	41.5	83.7[f]

[a]260 °C, 4 MPa H_2, LHSV = 0.3 h^{-1}, 2-ME. [b]260 °C, 4 MPa N_2, LHSV = 0.3 h^{-1}, 2-ME. [c]260 °C, 4 MPa H_2, LHSV = 0.3 h^{-1}, 2-ME. [d]270 °C, 4 MPa H_2, LHSV = 0.2 h^{-1}, ethanol. [e]220 °C, 5 MPa, propanols (*n*-propanol, 69.1% and isopropanol, 9.0%); [f]220 °C, 5 MPa, tetrahydropyran-2-methanol (75.5%) and 1,6-hexanediol (8.2%); H_2/substrate = 200 (mol/mol) for the cases in fix-bed reactor.

In the case of etherification, we use OM-Al_2O_3 catalyst for 2-ME synthesis with both H_2 and N_2 as carrier gas. A 2-ME yield of ∼65.8% was received when EG/methanol was used as a feed and H_2 was used as a carrier. N_2 greatly suppressed the side reactions and promoted 2-ME selectivity into 81.2%. When DMO was used as a feed, the C═O bonds need to be prereduced before etherification of C−O bonds. The 2Cu98Al catalyst with only 2% Cu gave 100% conversion and 66.9% 2-ME selectivity at a H_2 flow, revealing the high activity of the catalyst for the cascade hydrogenation−etherification reaction. In the case of hydrogenolysis, we received a high ethanol yield of ∼97.0% over the 15Cu85Al catalyst for EG hydrogenolysis. Then, we performed hydrogenolysis of 1,2-propandiol over this catalyst. A high conversion and total propanol selectivity were realized. The 15Cu85Al catalyst was further applied to hydrogenolysis of 1,2,6-hexanetriol, which is important for subsequent transformation of 5-hydroxymethylfurfural.[46] In this reaction, tetrahydropyran-2-methanol (2-THPM) is considered as the intermediate to access the high selectivity of 1,6-hexanediol. Because of the low efficiency of metal sites, the catalyst exhibited the conversion of ∼41.5%, a 2-THPM

dx.doi.org/10.1021/cs5009283 | ACS Catal. 2014, 4, 3612−3620

selectivity of ~75.5%, and a 1,6-hexanediol selectivity of ~8.2%. Compared with the noble-metal Rh−Re/SiO_2 catalyst (total metal loading of 12.5 wt %),[46] the 15Cu85Al catalyst (metal loading of 14.7 wt %) is still promising and worthy for further studies.

The above cases revealed that the catalyst design with proper exposed metal/acid sites can facilitate a given reaction toward object chemicals. The present work also furnished a one-pot strategy for metal/mesoporous Al_2O_3 bifunctional catalysts with plentiful pores, remarkable metal dispersion, and moderate acidity, which is promising for C═O, C−O, and O−H activation.

4. CONCLUSIONS

This paper describes the design of copper NP inlaid mesoporous Al_2O_3 catalysts with superior selectivity and lifespans for ethanol synthesis from DMO hydrogenation. A stable reactivity was realized via pinning Cu NPs in the stable mesoporous Al_2O_3 to prevent aggregation under the reaction conditions. The space restriction strategy demonstrated here conquers the deactivation of catalysts caused by metal aggregation and has potential values in other high-temperature and exothermic reactions. The catalysts also presented rich mesopores, highly dispersed Cu NPs, and moderate acidity. These desired features furnished the catalysts with high ethanol yields. The relationship that the intrinsic activity scales with the decreasing size of Cu NPs indicated a strong structure-sensitive behavior. The phenomenon can be attributed to the comprehensive effects of surface morphology, electronic structure of Cu NPs, Cu−Al_2O_3 interfacial sites, and balance of surface Cu^0−Cu^+ species for the metal−acid catalysts. A mechanism for ethanol generation from DMO hydrogenation (involves the activation of C═O, C−O, and O−H bonds) was also proposed. As EG represents a basic unit of bioderived molecules (polyols), the bifunctional catalysts were further used in converting the bioresources to various chemicals via hydrogenolysis of C−O bonds or etherification of O−H groups.

■ ASSOCIATED CONTENT

Supporting Information

Experimental details; Tables S1−S6; XRD of 15Cu85Al and Cu/mesoporous Al_2O_3 (Figure S1); TEM, STEM, and EDX images (Figures S2, S4−S6); TG results (Figure S3); FT-IR and Raman (Figure S7); pyridine adsorbed IR spectra (Figure S8); and Cu 2p XP and XAES spectra (Figures S9 and S10). This material is available free of charge via the Internet at http://pubs.acs.org.

■ AUTHOR INFORMATION

Corresponding Author

*E-mail: zhuyulei@sxicc.ac.cn. Tel.: +86 351 7117097. Fax: +86 351 7560668.

Author Contributions

Y.Z., X.K., and Y.Z. designed and performed the experiments and wrote the paper. X.L. and G.D. helped with some experiments and writing. Y.L. helped choose the model reactions.

Funding

This work was supported by the Major State Basic Research Development Program of China (973 Program; No. 2012CB215305).

Notes

The authors declare no competing financial interest.

■ ACKNOWLEDGMENTS

We would like to thank Dr. Fang Dong for the facilitation in the stability test and Dr. Bin Zhang for the helpful discussions.

■ REFERENCES

(1) Goldemberg, J. *Energy Environ. Sci.* **2008**, *1*, 523−525.
(2) Pereira, E. B.; Ramírez de la Piscina, P.; Martí, S.; Homs, N. *Energy Environ. Sci.* **2010**, *3*, 487−493.
(3) Gupta, M.; Smith, M. L.; Spivey, J. J. *ACS Catal.* **2011**, *1*, 641−656.
(4) Ramirez de la Piscina, P.; Homs, N. *Chem. Soc. Rev.* **2008**, *37*, 2459−2467.
(5) San, X.; Zhang, Y.; Shen, W.; Tsubaki, N. *Energy Fuels* **2009**, *23*, 2843−2844.
(6) Dexter, J.; Fu, P. *Energy Environ. Sci.* **2009**, *2*, 857−864.
(7) Lv, P.; Yuan, Z.; Wu, C.; Ma, L.; Chen, Y.; Tsubaki, N. *Energy Convers. Manage.* **2007**, *48*, 1132−1139.
(8) Gong, J.; Yue, H.; Zhao, Y.; Zhao, S.; Zhao, L.; Lv, J.; Wang, S.; Ma, X. *J. Am. Chem. Soc.* **2012**, *134*, 13922−13925.
(9) Wen, C.; Cui, Y.; Yin, A.; Fan, K.; Dai, W. L. *ChemCatChem.* **2013**, *5*, 138−141.
(10) Zhao, S.; Yue, H.; Zhao, Y.; Wang, B.; Geng, Y.; Lv, J.; Wang, S.; Gong, J.; Ma, X. *J. Catal.* **2013**, *297*, 142−150.
(11) Zhu, Y.; Zhu, Y.; Ding, G.; Zhu, S.; Zheng, H.; Li, Y. *Appl. Catal. A: Gen.* **2013**, *468*, 296−304.
(12) Yue, H.; Zhao, Y.; Zhao, S.; Wang, B.; Ma, X.; Gong, J. *Nat. Commun.* **2013**, *4*, 2339−2346.
(13) Bi, R.-R.; Wu, X.-L.; Cao, F.-F.; Jiang, L.-Y.; Guo, Y.-G.; Wan, L.-J. *J. Phys. Chem. C* **2010**, *114*, 2448−2451.
(14) Li, Y.; Wang, H.; Feng, Q.; Zhou, G.; Wang, Z.-S. *Energy Environ. Sci.* **2013**, *6*, 2156−2165.
(15) Schüth, F. *Chem. Mater.* **2014**, *26*, 423−434.
(16) Yin, A.; Wen, C.; Dai, W.-L.; Fan, K. *Appl. Catal., B* **2011**, *108−109*, 90−99.
(17) Yuan, Q.; Yin, A.-X.; Luo, C.; Sun, L.-D.; Zhang, Y.-W.; Duan, W.-T.; Liu, H.-C.; Yan, C.-H. *J. Am. Chem. Soc.* **2008**, *130*, 3465−3472.
(18) Morris, S. M.; Fulvio, P. F.; Jaroniec, M. *J. Am. Chem. Soc.* **2008**, *130*, 15210−15216.
(19) Xu, L.; Song, H.; Chou, L. *Catal. Sci. Technol.* **2011**, *1*, 1032−1042.
(20) Jiang, H.; Bongard, H.; Schmidt, W.; Schüth, F. *Microporous Mesoporous Mater.* **2012**, *164*, 3−8.
(21) Williams, W. D.; Shekhar, M.; Lee, W.-S.; Kispersky, V.; Delgass, W. N.; Ribeiro, F. H.; Kim, S. M.; Stach, E. A.; Miller, J. T.; Allard, L. F. *J. Am. Chem. Soc.* **2010**, *132*, 14018−14020.
(22) Shekhar, M.; Wang, J.; Lee, W. S.; Williams, W. D.; Kim, S. M.; Stach, E. A.; Miller, J. T.; Delgass, W. N.; Ribeiro, F. H. *J. Am. Chem. Soc.* **2012**, *134*, 4700−4708.
(23) Xu, Z.-N.; Sun, J.; Lin, C.-S.; Jiang, X.-M.; Chen, Q.-S.; Peng, S.-Y.; Wang, M.-S.; Guo, G.-C. *ACS Catal.* **2013**, *3*, 118−122.
(24) Cargnello, M.; Doan-Nguyen, V. V.; Gordon, T. R.; Diaz, R. E.; Stach, E. A.; Gorte, R. J.; Fornasiero, P.; Murray, C. B. *Science* **2013**, *341*, 771−773.
(25) Wu, C. T.; Qu, J.; Elliott, J.; Yu, K. M.; Tsang, S. C. *Phys. Chem. Chem. Phys.* **2013**, *15*, 9043−9050.
(26) Behrens, M.; Kasatkin, I.; Kühl, S.; Weinberg, G. *Chem. Mater.* **2010**, *22*, 386−397.
(27) Vazquez, A.; Lopez, T.; Gomez, R.; Morales, A.; Novaro, O. *J. Solid State Chem.* **1997**, *128*, 161−168.
(28) Cai, W.; Yu, J.; Jaroniec, M. *J. Mater. Chem.* **2011**, *21*, 9066−9072.
(29) Boumaza, A.; Favaro, L.; Lédion, J.; Sattonnay, G.; Brubach, J. B.; Berthet, P.; Huntz, A. M.; Roy, P.; Tétot, R. *J. Solid State Chem.* **2009**, *182*, 1171−1176.

(30) Layman, K. A.; Ivey, M. M.; Hemminger, J. C. *J. Phys. Chem. B* **2003**, *107*, 8538−8546.
(31) Chen, L.; Guo, P.; Qiao, M.; Yan, S.; Li, H.; Shen, W.; Xu, H.; Fan, K. *J. Catal.* **2008**, *257*, 172−180.
(32) Yin, A.; Guo, X.; Dai, W.; Fan, K. *J. Phys. Chem. C* **2009**, *113*, 11003−11013.
(33) Turek, W.; Haber, J.; Krowiak, A. *Appl. Surf. Sci.* **2005**, *252*, 823−827.
(34) Ruppert, A. M.; Weinberg, K.; Palkovits, R. *Angew. Chem., Int. Ed.* **2012**, *51*, 2564−2601.
(35) Natesakhawat, S.; Lekse, J. W.; Baltrus, J. P.; Ohodnicki, P. R.; Howard, B. H.; Deng, X.; Matranga, C. *ACS Catal.* **2012**, *2*, 1667−1676.
(36) Van Hardeveld, R.; Hartog, F. *Surf. Sci.* **1969**, *15*, 189−230.
(37) Mäki-Arvela, P.; Hájek, J.; Salmi, T.; Murzin, D. Y. *Appl. Catal., A* **2005**, *292*, 1−49.
(38) Shin, D.-W.; Dong, C.; Mattesini, M.; Augustsson, A.; Mao, S.; Chang, C. L.; Persson, C.; Ahuja, R.; Nordgren, J.; Wang, S. X.; Guo, J. H. *Chem. Phys. Lett.* **2006**, *422*, 543−546.
(39) Somorjai, G. A.; Contreras, A. M.; Montano, M.; Rioux, R. M. *Proc. Natl. Acad. Sci.* **2006**, *103*, 10577−10583.
(40) Rolison, D. R. *Science* **2003**, *299*, 1698−1701.
(41) Henry, C. R. *Surf. Sci. Rep.* **1998**, *31*, 231−325.
(42) Nakamura, I.; Fujitani, T.; Uchijima, T.; Nakamura, J. *J. Vac. Sci. Technol., A* **1996**, *14*, 1464−1468.
(43) Hu, Z.; Boyd, R. J. *J. Chem. Phys.* **2000**, *112*, 9562−9568.
(44) Behrens, M.; Studt, F.; Kasatkin, I.; Kühl, S.; Hävecker, M.; Abild-Pedersen, F.; Zander, S.; Girgsdies, F.; Kurr, P.; Kniep, B. L.; Tovar, M.; Fischer, R. W.; Nørskov, J. K.; Schlögl, R. *Science* **2012**, *336*, 893−897.
(45) Grabow, L. C.; Mavrikakis, M. *ACS Catal.* **2011**, *1*, 365−384.
(46) Buntara, T.; Noel, S.; Phua, P. H.; Melian-Cabrera, I.; de Vries, J. G.; Heeres, H. J. *Angew. Chem., Int. Ed.* **2011**, *50*, 7083−7087.